# Salt Reconstruction in Full Waveform Inversion with a Parametric Level-Set Method

A. Kadu, T. van Leeuwen and W. A. Mulder

*Abstract*—Seismic full-waveform inversion tries to estimate subsurface medium parameters from seismic data. Areas with subsurface salt bodies are of particular interest because they often have hydrocarbon reservoirs on their sides or underneath. Accurate reconstruction of their geometry is a challenge for current techniques. This paper presents a parametric level-set method for the reconstruction of salt-bodies in seismic full-waveform inversion. We split the subsurface model in two parts: a background velocity model and the salt body with known velocity but undetermined shape. The salt geometry is represented by a level-set function that evolves during the inversion. We choose radial basis functions to represent the level-set function, leading to an optimization problem with a modest number of parameters. A common problem with level-set methods is to fine tune the width of the level-set boundary for optimal sensitivity. We propose a robust algorithm that dynamically adapts the width of the level-set boundary to ensure faster convergence. Tests on a suite of idealized salt geometries show that the proposed method is stable against a modest amount of noise. We also extend the method to joint inversion of both the background velocity model and the salt-geometry.

*Index Terms*—Level set, Inverse problem, Seismology

## I. Introduction

SEISMIC imaging attempts to obtain detailed images of the subsurface from seismic data. Such data are obtained by placing explosive or other types of sources on or near the surface and recording the response with a large array of receivers at the surface. By repeating the experiment many times for different source positions, enough data can be gathered to form useful images. The scale of these experiments varies from tens of meters, for instance, for near-surface imaging, to tens of kilometers in oil and gas exploration, up to the whole Earth in global seismology. For hydrocarbon exploration, depths typically extend to several kilometers.

One of the main challenges of seismic imaging is that the propagation velocity of the seismic waves traveling through the subsurface is unknown. Since this velocity can vary significantly, both laterally and with depth, it has to be estimated prior to applying a conventional imaging method. A wrong subsurface velocity can lead to severely distorted images. The conventional workflow for seismic imaging, therefore, is to first estimate the subsurface velocity and subsequently back-propagate the data to obtain an image. The success of this two-step approach relies crucially on the ability to isolate the reflection events in the data. This can only be done if the earth structure is relatively simple, e.g. smoothly varying

Ajinkya Kadu and Tristan van Leeuwen are with the Mathematical Institute, Utrecht University, The Netherlands. Wim Mulder is associated with Delft University of Technology, The Netherlands and Shell Global Solutions International B.V.

with small perturbations. A particularly relevant setting in which the separation-of-scales argument fails to hold is in the presence of strong contrasts, such as salt diapirs, salt slabs, anhydrite or basalt layers. Salt geometries are of particular interest because they often have hydrocarbon reservoirs on their sides or underneath.

Full-waveform inversion (FWI) attempts to fit the data using a fairly precise numerical model for wave-propagation in heterogeneous media [15], [37], [55]. By posing the inverse problem as a non-linear least-squares problem, the velocity structure in the subsurface can, in principle, be estimated quantitatively. However, this optimization problem is severely non-linear and ill-posed, making it very difficult to obtain reasonable results without a good initial guess of the velocity parameters. Starting from an initial guess that is far away from the truth often leads to an incorrect subsurface model. While many approaches have been proposed to mitigate this problem, the issue remains unsolved [8], [35], [51], [53].

In this paper, we aim to alleviate the ill-posedness of the problem to some extent by adding an appropriate regularization. In the particular setting of salt bodies, it is reasonable to assume that the subsurface can be described as one or more continuous bodies (salt) with known constant material parameters, surrounded by continuously varying parameters (sediment). Our approach is based on a level-set method, where we implicitly represent the shape of the salt body with a level-set function. By expanding the level-set function in some basis, we greatly reduce the effective number of parameters and obtain a non-linear optimization problem that is better behaved than the original non-linear least-squares problem.

The paper is organized as follows. In Section II, we review the details of the classical FWI approach and give an overview regularization approaches specifically aimed at the reconstruction of salt bodies. In Section III, we present the basics of the parametric level-set method and discuss several practical issues in detail. Numerical results on a stylized seismic example are presented in Section IV. Finally, Section V concludes the paper.

## II. Full Waveform Inversion

Full waveform inversion (FWI) is non-linear data-fitting scheme aiming to retrieve detailed estimates of subsurface properties from seismic data. The basic workflow of FWI is as follows: *(1)* predict the observed data by solving a wave-equation, given an initial guess of the subsurface velocity, *(2)* compute the difference between predicted and observed data, and *(3)* update the velocity in order to improve the data fit. This process is repeated in an iterative fashion until the residual

drops below some tolerance. An excellent overview of various flavors of this basic scheme can be found in [55].

There are several ways to model seismic wave propagation, in either the frequency or time domain. We refer the reader to the reviews by [9] and [54]. For our purpose, it suffices to consider a two-dimensional scalar Helmholtz equation that models the acoustic pressure:

$$\omega^2 m(\mathbf{x})u(\omega,\mathbf{x}) + \nabla^2 u(\omega,\mathbf{x}) = q(\omega,\mathbf{x}), \qquad (1)$$

where $\mathbf{x} \in \mathbb{R}^2$ denotes the subsurface position, $m(\mathbf{x})$ is the squared slowness with units $s^2/m^2$, $\omega$ is the angular frequency, $q$ the source term and $u$ the pressure wavefield. We consider an unbounded domain and impose Sommerfeld radiation conditions [4]. The observed data are modeled by solving (1) for several sources $\{q_i\}_{i=1}^{n_s}$ and sampling the resulting wavefields $u_i$ at locations $\{\mathbf{x}_j\}_{j=1}^{n_r}$ and frequencies $\{\omega_k\}_{k=1}^{n_f}$, i.e.,

$$d_{ijk} = u_i(\omega_k, \mathbf{x}_j).$$

The inverse problem is now to retrieve $m(\mathbf{x})$ from a set of observations $d_{ijk}$. This problem has been extensively studied and uniqueness results are available for a few specific cases, including layered earth-models, small perturbations around a known smooth reference medium and asymptotic versions of the problem. We refer to [49] for an extensive overview.

### A. Discretization and optimization

A common approach to the inverse problem is to first discretize and solve the wave equation for forward modelling and to subsequently formulate a finite-dimensional data-fitting problem.

A finite-difference discretization of (1) on an $N$-point grid with absorbing boundary conditions leads to a sparse system of equations

$$A(\omega,\mathbf{m})\mathbf{u} = \mathbf{q},$$

where $A \in \mathbb{C}^{N \times N}$ is structurally symmetric and indefinite. Various dispersion-minimizing finite-difference stencils have been proposed in the literature [20], [45], [52] and several absorbing boundary conditions are described in [10] and [11].

The system of equations can be solved by a decomposition of $A$ such as the LU (lower and upper triangular) decomposition. The advantage of this direct approach is that, once the decomposition has been performed, the system can be solved efficiently for multiple sources by forward and backward substitution [25], [27]. The direct approach with nested dissection [16] is efficient for 2-D problems [19], [20], [48]. However, the time and memory complexities of LU factorization and its limited scalability on large-scale distributed memory platforms prevent its application to large-scale 3-D problems that may involve more than 10 million unknowns [31]. Helmholtz-specific factorization methods have been developed [56], but these are only suitable when the computational cost can be amortized over many sources.

Iterative solvers provide an alternative approach for solving the Helmholtz equation [12], [21], [34], [39]. These iterative solvers are usually implemented with Krylov subspace methods [41] that are preconditioned by solving a damped Helmholtz equation. The solution of the damped equation is computed efficiently with a multigrid method. The main advantage of the iterative approach is the low memory requirement, although the main drawback results from the difficulty to design an efficient preconditioner because $A$ is indefinite [13]. Also, the iterative scheme has to be started again for each source.

Organizing the observations in a vector $\mathbf{d} \in \mathbb{C}^M$ with $M = n_s n_r n_f$, we introduce the forward operator

$$\mathbf{d} = F(\mathbf{m}).$$

Application of the forward operator on a given model $\mathbf{m}$ involves the solution of $n_f n_s$ Helmholtz equations, including the LU decompositions, and constitutes the main computational cost of FWI.

The conventional least-squares formulation of FWI can now be expressed as

$$\min_{\mathbf{m}}\{f(\mathbf{m}) = \tfrac{1}{2}\|F(\mathbf{m}) - \mathbf{d}\|_2^2\}. \qquad (2)$$

This optimization problem is typically solved with a Newton-like algorithm [38]:

$$\mathbf{m}_{k+1} = \mathbf{m}_k - \lambda_k H_k^{-1}\nabla f(\mathbf{m}_k),$$

where $\lambda_k$ is the step size and $H_k$ denotes (an approximation of) the Hessian of $f$ at iteration $k$. The gradient of the objective is given by

$$\nabla f(\mathbf{m}) = J(\mathbf{m})^*(F(\mathbf{m}) - \mathbf{d}),$$

where $J(\mathbf{m})$ is the Jacobian of $F$ and $J^*$ denotes its adjoint or conjugate transpose. In practice, the Jacobian matrix is never formed explicitly but its action is computed using the *adjoint-state method* [18]. This entails solving $n_s n_f$ linear systems with $A^*$ and the residual as right-hand sides. The action of the (Gauss-Newton) Hessian may be computed in a similar fashion at the cost of additional Helmholtz-solves [38]. This can be done cheaply in 2D if the LU factors are kept in memory while needed [29].

### B. Ill-posedness and local minima

Unfortunately, waveform inversion is hampered by the presence of local minima in $f$ [42]. In practice, this requires a good initial estimate of the parameters $\mathbf{m}$. To circumvent this problem, the data can be inverted in a multi-scale fashion, starting at some lowest frequency available in the data and using the inversion result to initialize a next pass at a higher frequency [8], [47]. The low frequencies are important in reconstructing the large-scale variations in the model, while high frequencies fill in the details [6]. All of these will fail, however, when the initial guess does not explain the observations well enough for the lowest available frequency.

Many alternative formulations have been proposed that depart from the usual data-fitting approach [5], [35], [50], [51], [53]. While these approaches can to some extent mitigate the non-linearity of the problem, they do not solve the inherent ill-posedness of the problem. This means that some features of $\mathbf{m}$ are simply not recoverable, regardless of the method we use to estimate the parameters. To address this problem, we need to add regularization.

## C. Regularization

We distinguish two types of regularization: *implicit* regularization, where we add a penalty $\rho(\mathbf{m})$ to the objective in (2) to penalize unwanted features, and *explicit* regularization, where we expand $\mathbf{m}$ in an appropriate basis that contains only the features we desire. For example, when we expect the model to vary smoothly, we can penalize the second derivative by a penalty term

$$\rho(\mathbf{m}) = \|L\mathbf{m}\|_2^2,$$

with $L$ the discrete Laplace operator. Alternatively, we can choose a representation of the form

$$\mathbf{m} = B\mathbf{a},$$

where $B$ consists of smooth basis functions such as B-splines. This type of regularization works well when the scales of the model are separable, since we can invert for a smoothly varying velocity from low-frequency data [8].

In some geological settings, however, the scales do *not* separate, and we need to find an alternative form of regularization. If we expect our model to have strong discontinuities, a popular choice is a Total-Variation (TV) regularization with $\rho(\mathbf{m}) = \|D\mathbf{m}\|_1$, with $D$ a discrete gradient operator [24], [40]. A natural basis is hard to define in this case. Alternatively, we can regularize the model by imposing the constraint $\|D\mathbf{m}\|_1 \leq \tau$ [14].

A disadvantage is that TV regularization acts globally and causes the model to be blocky everywhere. Nevertheless, some promising results have been obtained recently [2], [3], [14].

As an alternative to TV regularization, a level-set method for waveform inversion in the presence of salt-bodies has been considered by [17], [23]. For completeness sake and to set the notation, we first give a brief overview of the classical level-set approach and then introduce our approach.

## III. LEVEL-SET METHOD

We represent $m(\mathbf{x})$ as being constant in a certain region and continuously varying elsewhere. We start again from the continuous formulation of the inverse problem and derive a finite-dimensional optimization problem analogous to (2). We represent $m$ as

$$m(\mathbf{x}) = \begin{cases} m_1 & \text{if } \mathbf{x} \in \Omega, \\ m_0(\mathbf{x}) & \text{otherwise.} \end{cases}$$

Here, $\Omega$ indicates the salt-body, $m_1$ is the constant value of the model parameter inside the salt body and $m_0(\mathbf{x})$ denotes the spatially varying parameters in the sediment. Fig. 1 sketches three different models, representing the smooth variation, blocky structure and a combination of both. Model 1 is a typical sediment structure, while model 2 represents the salt geometry. We generally expect a seismic velocity distribution similar to model 3, combining model 1 and 2.

We can represent the model formally as

$$m(\mathbf{x}) = [1 - \chi_\Omega(\mathbf{x})]m_0(\mathbf{x}) + \chi_\Omega(\mathbf{x})m_1,$$

where $\chi_\Omega(\mathbf{x})$ is the indicator function of $\Omega$. The inverse problem now consists of finding the set $\Omega$ and the model
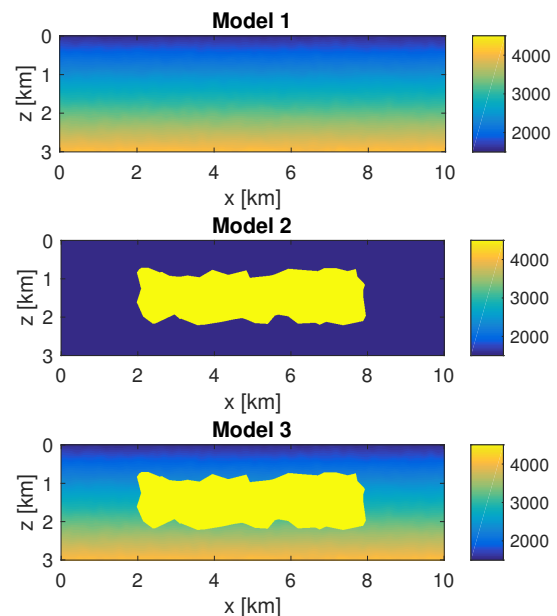


Fig. 1. Model 1: smooth velocity variation (sediment). Model 2: random 2D body with higher velocity (salt). Model 3: combination of smooth variation and blocky model. All velocities in $m/s$.

parameters $m_0(\mathbf{x})$ and $m_1$. The basic idea behind the level-set method is to represent the domain $\Omega$ through a level-set function as $\Omega = \{\mathbf{x} \,|\, \phi(\mathbf{x}) \geq 0\}$ [28], [32]. This then leads us to represent the indicator function as $\chi_\Omega(\mathbf{x}) = h(\phi(\mathbf{x}))$, where $h$ is the Heaviside function $h(s) = (1 + \text{sign}(s))/2$.

To be able to compute sensitivities, one typically uses a smooth approximation of the Heaviside function. A common choice is

$$h_\varepsilon(s) = \frac{1}{1 + e^{-s/\varepsilon}},$$

where $h_\varepsilon \to h$ as $\varepsilon \to 0$. This function has the nice property that its derivative is non-zero everywhere. A disadvantage is that, in order to accurately represent the indicator function, the level-set function $\phi$ will need to tend to $\pm\infty$. This induces very steep gradients in $\phi$ around the boundary of the level-set. In turn, these steep gradients in $\phi$ require that we pick a proportionally large $\varepsilon$ to remain sensitive to changes in the level-set. This suggest that we pick $\varepsilon$ in accordance with the (maximum) gradient of $\phi$. We will get back to this observation in Section III-C.

To avoid some of these issues, we use a smooth Heaviside defined by

$$h_\varepsilon(s) = \begin{cases} 0 & \text{if } s < -\varepsilon, \\ \frac{1}{2}\left[1 + \frac{s}{\varepsilon} + \frac{1}{\pi}\sin(\frac{\pi s}{\varepsilon})\right] & \text{if } -\varepsilon \leq s \leq \varepsilon, \\ 1 & \text{if } s > \varepsilon. \end{cases}$$

To avoid getting trapped in the region where $h_\varepsilon' = 0$, we again have to pick $\varepsilon$ in accordance with the (maximum) gradient of $\phi$. A practical heuristic to pick $\varepsilon$ and adapt it to the current $\phi$ will be discussed in Section III-C.

The level-set method was originally introduced for tracking regions in fluid flow applications, providing a natural way to evolve the level-set by solving a Hamilton-Jacobi equation

[33]. In applications like FWI, it is not obvious how to update $\phi$ away from the boundary of $\Omega$, because $h'_\varepsilon(x)$ quickly tends to zero. The problem of finding the level-set function is ill-posed.

### A. A parametric level-set approach

We adopt a method proposed in [1] and represent the level-set function with a finite set of radial basis functions (RBFs):

$$\phi(\mathbf{x}) = \sum_{i=1}^{L} \alpha_i \Psi(\beta \|\mathbf{x} - \xi_i\|_2),$$

where $\Psi(r)$ is a RBF, $\xi_i$ are the nodes and $\beta$ is a scaling parameter. The choice of RBF will be discussed in more detail in the next subsection.

Discretization on an $N$-point grid leads to the so-called RBF-kernel matrix $K \in \mathbb{R}^{N \times L}$ with elements $k_{ij} = \Psi(\beta \|\mathbf{x}_i - \xi_j\|_2)$, allowing us to represent the parameters as

$$\mathbf{m}(\mathbf{m}_0, m_1, \alpha) = \mathbf{m}_0 \odot (\mathbf{1} - h_\varepsilon(K\alpha)) + m_1 h_\varepsilon(K\alpha), \quad (3)$$

where $\odot$ represents element-wise multiplication, also known as the Hadamard product. We can now define the corresponding optimization problem for the parametric level-set approach, for fixed $\mathbf{m}_0, m_1$, as minization over the cost functional

$$\widetilde{f}(\alpha) = \tfrac{1}{2} \|F(\mathbf{m}(\alpha)) - \mathbf{d}\|_2^2. \quad (4)$$

The gradient of this objective is given by

$$\nabla \widetilde{f}(\alpha) = \left(\frac{\partial \mathbf{m}}{\partial \alpha}\right)^T \nabla f(\mathbf{m}(\alpha)), \quad (5)$$

where

$$\frac{\partial \mathbf{m}}{\partial \alpha} = \text{diag}\left\{ (m_1 \mathbf{1} - \mathbf{m_0}) \odot h'_\varepsilon(K\alpha) \right\} K.$$

### B. Radial basis functions

Radial basis functions are a means to approximate smooth multivariate functions. They have been extensively studied in the context of the interpolation of scattered data in high dimensions and for meshless methods [7], [36], [58]. RBFs are classified into two main types, global RBFs, which have infinite support, and compactly supported RBFs. Next, we discuss some relevant properties when we consider approximating a given smooth function $\phi$ using RBFs.

*1) Global RBFs:* Global RBFs have infinite support and hence the RBF kernel matrix $K$ is dense. An overview of several common global RBFs is given in Table I and their radial behavior is shown in Fig. 2. For the multiquadric, the kernel matrix is positive definite [26]. Among the advantages of global RBFs are (1) highly accurate and often exponentially convergent, (2) easy applicable to high-dimensional problems, (3) meshless in the approximation of multivariate scattered data and (4) numerical accuracy is easily improved by adding more points in regions with large gradients.

However, the corresponding interpolation matrix is dense and ill-conditioned and therefore sensitive to the shape parameter. As a result, the application of traditional RBF interpolation to large-scale problems is computationally expensive.

TABLE I
GLOBAL RBFs.

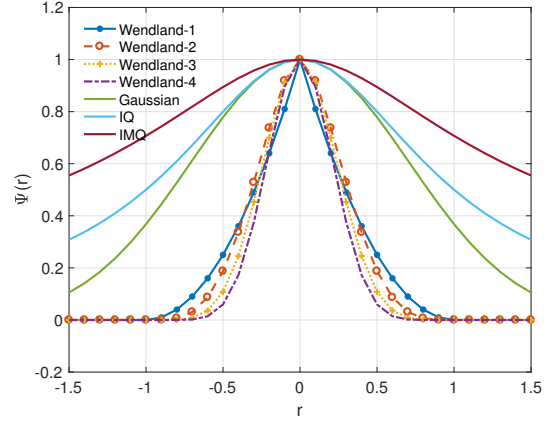| Name | $\Psi(r)$ |
|---|---|
| Gaussian | $\exp(-r^2)$ |
| Multiquadric | $\sqrt{1 + r^2}$ |
| Inverse multiquadric (IMQ) | $\frac{1}{\sqrt{1+r^2}}$ |
| Inverse quadratic (IQ) | $\frac{1}{1+r^2}$ |



Fig. 2.  Various types of global and compact (Wendland) RBF.

*2) Compactly supported RBF:* These result in a sparse, positive definite, and generally better conditioned kernel matrix [57]. However, the order of approximation is usually less than with global RBFs. Table II provides an overview of some common compactly supported RBFs. Fig. 2 presents their radial behavior.

### C. Shape representation

To determine which type of RBF is most suitable for our purpose, we study how well we can represent typical salt bodies with various RBFs. These salt models are discretized on a cartesian grid with grid spacing $h$. We choose the nodes of the RBFs on a cartesian grid with a larger grid spacing $h_r = 5h$ and normalize the scale parameter for the compactly supported RBFs with $\beta = \frac{1}{\gamma h_r}$.

We determine the coefficients $\alpha$ by solving

$$\min_\alpha \tfrac{1}{2} \|h_\varepsilon(K_\gamma \alpha) - \mathbf{m}\|_2^2,$$

with a L-BFGS method [30]. Results for the Wendland-4 RBF with $\gamma = 4$ and $\varepsilon = 10^{-1}$ are shown in Fig. 3(a–d). The lower-order Wendland RBFs gave a less good approximation. Results with the global RBFs are similar to those of the compact ones.

TABLE II
WENDLAND COMPACTLY-SUPPORTED RBFs. HERE, $k$ DENOTES THE
ORDER OF SMOOTHNESS (I.E., $\phi$ IS K TIMES CONTINUOUSLY
DIFFERENTIABLE).

| Name | $\Psi(r)$ | $k$ |
|---|---|---|
| Wendland-1 | $(1-r)_+^2$ | 0 |
| Wendland-2 | $(1-r)_+^4(4r+1)$ | 2 |
| Wendland-3 | $(1-r)_+^6(35r^2+18r+3)$ | 4 |
| Wendland-4 | $(1-r)_+^8(32r^3+25r^2+8r+1)$ | 6 |

As noted earlier in Section III, we need to pick $\varepsilon$ in accordance with the gradient of level-set function in order to have optimal sensitivity. We propose to choose $\varepsilon$ adaptively based on the (fraction) of upper bound on the gradient. It is represented as

$$\varepsilon = \kappa \left[ \max(K_\gamma \alpha) - \min(K_\gamma \alpha) \right]. \qquad (6)$$

This choice of $\varepsilon$ with $\kappa = 5 \times 10^{-2}$ produced the results in Fig. 3(e–h).

### D. Algorithm

Algorithm 1 summarizes parametric level-set full waveform inversion (PLS-FWI). This method introduces a small, $\mathcal{O}(N)$ flops overhead compared the the conventional FWI approach. This is negligible compared to the $\mathcal{O}(N^{(3/2)})$ complexity of solving the Helmholtz equation in 2D with nested dissection.

---

**Algorithm 1** PLS-FWI Basic Algorithm

---

**Input:** Data $\mathbf{d} \in \mathbb{R}^{n_s \times n_r \times n_f}$, estimate of background parameter $\mathbf{m_0}$, salt parameter $m_1$, initial estimate of weights $\alpha$, $\kappa$
**Output:** final weights $\alpha$, model $\mathbf{m}$
  1: **for** $j = 1$ to itermax **do**
  2:     compute Heaviside $\varepsilon$ from equation (6)
  3:     compute misfit $\widetilde{f}(\alpha)$ from equation (4) and gradient $\nabla \widetilde{f}(\alpha)$ from equation (5)
  4:     $\alpha \leftarrow \alpha + \lambda \widetilde{H}^{-1} \nabla \widetilde{f}(\alpha)$
  5: **end for**
  6: compute $\mathbf{m}$ from equation (3).

---

Algorithm 2 outlines the multi-scale approach of PLS-FWI. We reduce $\kappa$ for Heaviside $\varepsilon$ after every frequency band to decrease the size of level-set boundary. The idea is to start optimization with large boundary (high $\kappa$) and small initial level-set to capture large sensitivity, allowing for large updates. Decreasing the level-set boundary then provides sharper images.

---

**Algorithm 2** PLS-FWI Multi-scale Algorithm

---

**Input:** Data in frequency batches $\{\mathbf{d}_1, \mathbf{d}_2, \dots \mathbf{d}_n\}$, estimate of background parameter $\mathbf{m_0}$, salt parameter $m_1$, initial estimate of weights $\alpha_0$
**Output:** model $\mathbf{m}$
  1: $\kappa \leftarrow 0.1$
  2: **for** $i = 1$ to $n_{\text{batches}}$ **do**
  3:     $\alpha_i \leftarrow \text{PLS-FWI}(\mathbf{d}_i, \mathbf{m_0}, m_1, \alpha_{i-1}, \kappa)$
  4:     $\kappa \leftarrow 0.8 \times \kappa$
  5: **end for**
  6: $\varepsilon \leftarrow 0$
  7: compute $\mathbf{m}$ from equation (3).

---

## IV. Results

To demonstrate the capabilities of the parametric level-set full waveform inversion, we perform simulations on four different velocity models. These models are shown in Fig. 4. Each has a background velocity increasing linearly with depth as $1500 + bz$ with $b = 0.8333$. The salt bodies in these model have a constant velocity of 4500 m/s. We choose a grid spacing of 50 m in each direction, providing a total of $N = 201 \times 61$ grid points.

The acquisition setup is shown in Fig. 5, with 50 sources placed at top of the model and 100 receivers placed at the depth of 50 m. Also shown is the part of the model to which the data are most sensitive. Features of the model in the lower left and right corners are hard to recover because of the limited aperture.

We use a frequency-domain finite-difference code [46] to generate the data for frequencies between 2.5 and 3.5 Hz with a spacing of $6.25 \times 10^{-2}$ Hz. The data are weighted in frequency by a Ricker wavelet with a peak frequency of 15 Hz. For the inversion, we select four bands, $[2.5 - 2.75]$ Hz, $[2.75 - 3.0]$ Hz, $[3.0 - 3.25]$ Hz and $[3.25 - 3.5]$ Hz, each with 4 four frequencies.

For PLS-FWI, the RBF grid has a spacing of 250 m in both directions. As shown in Fig. 6, two extra layers of RBF nodes are added outside the physical domain to provide flexibility in reconstructing the level-set near the boundary. We use a fourth-order Wendland RBF with $\gamma = 4$ and choose $\varepsilon$ adaptively as described in Section III-C. We found that $\varepsilon$ usually stabilizes after the first few iterations.

We compare FWI and PLS-FWI on noise-free and on data with white noise, with an SNR of 10dB. Finally, we perform a joint reconstruction of both the salt geometry and the background model $\mathbf{m}_0 = 1500 + bz$, parametrized by the slope $b$.

For FWI, we use a projected Quasi-Newton method [44] to solve the resulting optimization problem with bound-constraints on $\mathbf{m}$ to ensure that the velocity stays within the feasible range of $[1500, 4500]$ m/s. To solve the resulting optimization problem in $\alpha$ (PLS-FWI), we rely on the L-BFGS approximation of the Hessian [43]. We perform 150 iterations per frequency band while resetting the L-BFGS memory after handling each frequency band. For joint salt and background reconstruction with PLS-FWI, we use a bisection method to find the optimal $b$.

### A. Salt geometry determination

The initial model for conventional FWI and the background model for PLS-FWI are taken to be the same, linearly increasing velocity models as in the true ones. For PLS-FWI, we let $m_1$ correspond to the true velocity in the salt and initialize the level-set as shown in Fig. 6. For model B, we initialize the level-set function with two positive regions near the top of the two salt bodies.

*1) Noise-free data:* Fig. 7a, 7c, 7e and 7g show the reconstructed models using FWI. To a large extent, the results predict the top of the salt but fail to identify its proper shape. They also include some artefacts, as shown in the left bottom part of Fig. 7g. On the other hand, PLS-FWI almost perfectly recovers the salt geometry in each of the models, as can be seen in Fig. 7b, 7d, 7f and 7h. These models retain their sharpness even with low frequencies because we reduce $\varepsilon$ to zero in step 6 of algorithm 2.
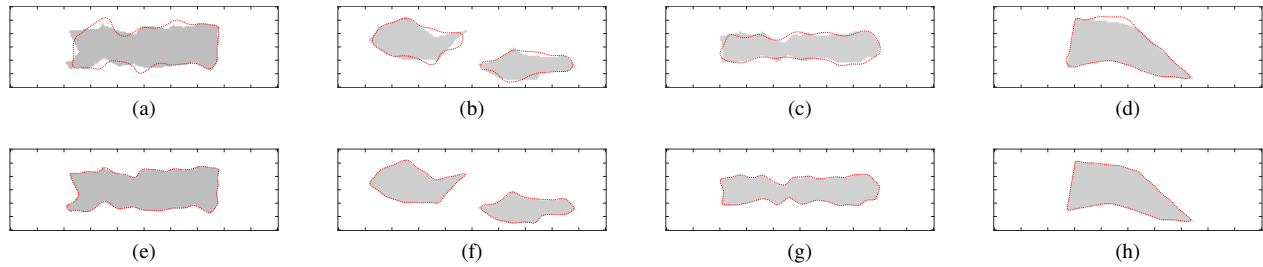
Fig. 3. (a), (b), (c), (d) show level-set reconstructions of salt geometries with fixed $\varepsilon = 0.1$, while (e), (f), (g), (h) reveal the improved reconstructions with new formulation of $\varepsilon$ presented in equation (6) (red dotted line denotes the reconstructed zero contour of the level-set).
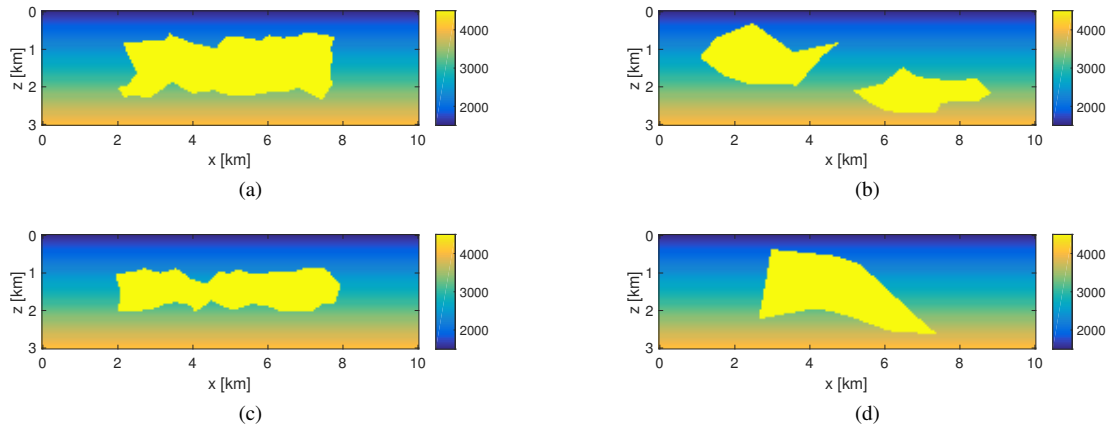
Fig. 4. Velocity models (in m/s) created for the inversion test. They are referred to as model A (a), model B (b), model C (c) and model D (d).
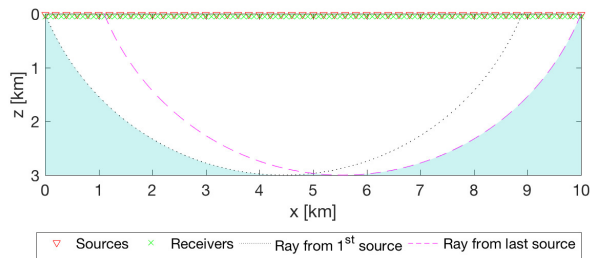
Fig. 5. Source and receivers for the simulation. Sources are placed on top, receivers at a depth of 50 m. The two ray paths separate the region recoverable by inversion from the shaded non-recoverable part [22].
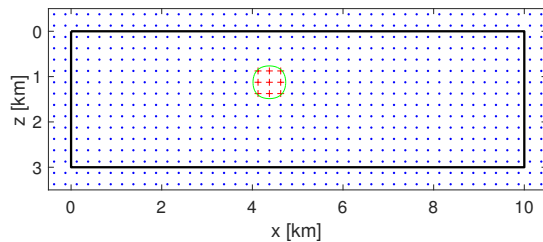
Fig. 6. Placements of RBF on the computational grid (denoted by thick black line). To initialize the zero contour of the level set (green line) that defines the salt body, a few RBFs around the center have been allocated positive values (denoted by red plusses), others are negative (denoted by blue dots).

To compare the proposed method with conventional FWI,

TABLE III
COMPARISON OF MISFIT AND RRE VALUES FOR CLASSICAL FWI VS PLS-FWI

| Model | ERF | | RRE | |
|---|---|---|---|---|
| | FWI | PLS-FWI | FWI | PLS-FWI |
| A | 0.0281 | $5.8197 \times 10^{-4}$ | 0.8213 | 0.0707 |
| B | 0.0221 | $2.9183 \times 10^{-4}$ | 0.8072 | 0.0856 |
| C | 0.0261 | $4.7127 \times 10^{-4}$ | 0.9102 | 0.0732 |
| D | 0.0339 | $9.0299 \times 10^{-6}$ | 0.8088 | 0.0434 |

we define the error reduction factor (ERF),

$$\text{ERF}_{\text{recon}} = \frac{\|F(\mathbf{m}_{\text{recon}}) - \mathbf{d}\|_2}{\|F(\mathbf{m}_0) - \mathbf{d}\|_2}.$$

An ERF close to the best achievable ERF (0 in case of noise-free data) indicates a better performance of the reconstruction method in reducing the data misfit. Table III shows the improvement in the data misfit with PLS-FWI over classic FWI. The data misfit is reduced by a factor $10^{-4}$ on average with the use of PLS-FWI.

To compare the reconstructions for different methods, we define a measure called the Relative Reconstruction Error (RRE) as

$$\text{RRE}_{\text{recon}} = \frac{\|\mathbf{m}_{\text{recon}} - \mathbf{m}_{\text{true}}\|_2}{\|\mathbf{m}_0 - \mathbf{m}_{\text{true}}\|_2},$$

where $\mathbf{m}_{\text{recon}}$ is the model reconstructed by FWI or PLS-FWI. From Table III, we observe that the RRE is reduced dramatically with PLS-FWI.
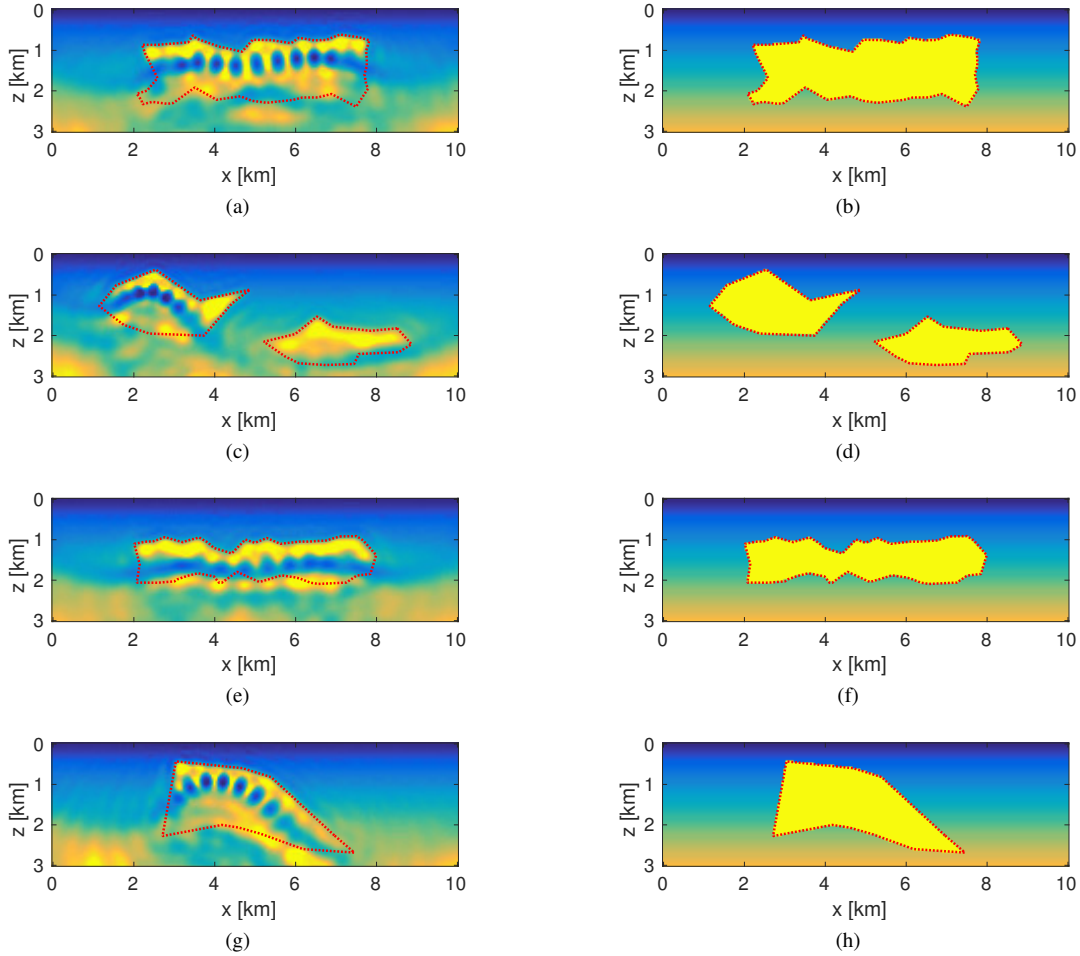
Fig. 7.  Salt reconstruction with classical FWI and parametric level-set full waveform inversion (PLS-FWI) from noise free data. (a), (c), (e) and (g) represent models A, B, C, and D, reconstructed with classical full waveform inversion. (b), (d), (f) and (h) represent reconstructed model A, B, C, D using PLS-FWI. The red dotted line shows the true geometry of salt.

*2) Noisy data:* Fig. 8a, 8c, 8e and 8g show the reconstructed models using FWI while Fig. 8b, 8d, 8f, 8h show the models reconstructed by PLS-FWI. The results are essentially the same as for the noise-free case, except for some artifacts outside the region of interest in the PLS-FWI results. Fig. 9 exhibit the variation of achieved level-set function for Model A. The gradient near the left bottom corner still is large, suggesting the method has difficulty in getting rid of the incorrect salt geometry.

Table IV shows the improvement in the data misfit with PLS-FWI over classic FWI. For noisy data, we also look at the best achievable ERF, which is defined as

$$\text{ERF}_{\text{achievable}} = \frac{\|F(\mathbf{m}_{\text{true}}) - \mathbf{d}\|_2}{\|F(\mathbf{m}_0) - \mathbf{d}\|_2}.$$

This quantity denotes the smallest ERF achievable by any reconstruction method. The ERF for PLS-FWI is closer to the best achievable ERF than that of FWI. With the classic approach, the relative reconstruction error is slightly affected when noise is added to data. On the other hand, RRE changes by a large factor in the presence of noise with the proposed method. The false salt geometries mainly attribute to these large changes.

TABLE IV
COMPARISON OF MISFIT AND RRE VALUES FOR CLASSIC FWI VS. PLS-FWI (NOISY DATA).

| Model | ERF | | | RRE | |
|---|---|---|---|---|---|
| | FWI | PLS-FWI | achievable | FWI | PLS-FWI |
| A | 0.5425 | 0.5254 | 0.5246 | 0.8432 | 0.2437 |
| B | 0.6172 | 0.5956 | 0.5950 | 0.8332 | 0.2085 |
| C | 0.6090 | 0.5958 | 0.5951 | 0.9199 | 0.1817 |
| D | 0.5530 | 0.5325 | 0.5321 | 0.8239 | 0.1382 |

### B. Simultaneous reconstruction of salt and background

Next, we jointly reconstruct the salt geometry and the background, parametrized by $b$. For each frequency band, we first estimate the optimal $b$, for fixed $\alpha$ and setting $\varepsilon = 0$, using a bisection method and subsequently estimate the salt geometry with PLS-FWI (Algorithm 1). The bisection method is initialized with the interval $[0, 1]$ for $b$.

Fig. 10a, 10b, 10c and 10d show the reconstructed models for noisy data. The salt geometry is accurately predicted, but contains a few artifacts. Table V indicates the predicted values of $b$ in each of the models, which are very close to true value
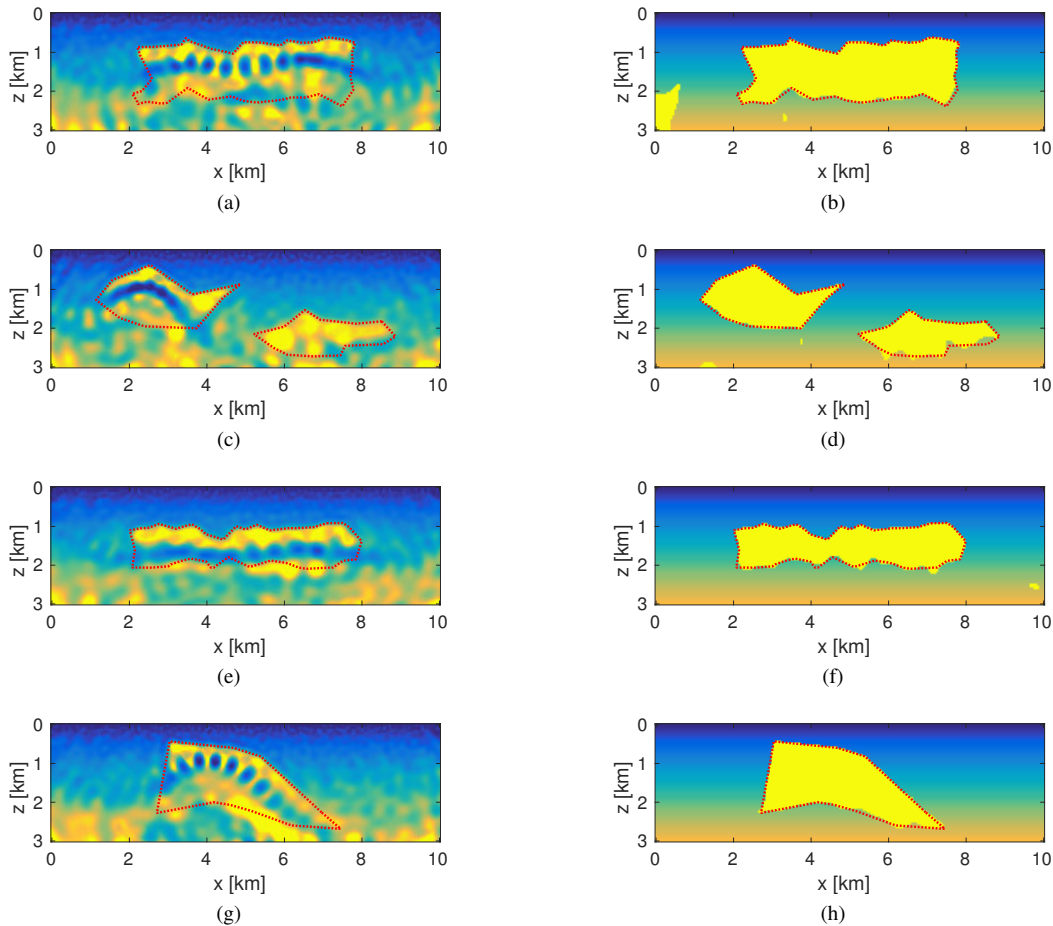
Fig. 8. Salt reconstruction with classic FWI and Parametric level-set full waveform inversion (PLS-FWI) with noisy data of SNR 10 *dB*. (a), (c), (e), (g) represent reconstructed model A, B, C, D with classic full waveform inversion respectively. (b), (d), (f), (h) represent reconstructed model A, B, C, D with PLS-FWI respectively. Red dotted line shows the true geometry of salt.
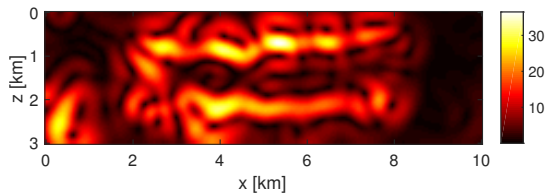


Fig. 9. Gradient of the final level set function for model A with noisy data.

TABLE V
RECOVERED VALUES OF $b$ FOR DIFFERENT MODELS (NOISY DATA).

| Model | A | B | C | D |
|-------|-------|-------|-------|-------|
| $b$ | 0.8351 | 0.8351 | 0.8345 | 0.8333 |

of $b = 0.8333$.

## V. DISCUSSIONS AND CONCLUSION

Accurately determining the geometry of subsurface salt bodies from seismic data is a difficult problem. When casting the inverse problem into a non-linear data-fitting problem, both the presence of local minima and the ill-posedness of the problem prevent accurate recovery of the salt-geometry.

We have investigated the application of a parametric level-set method to address this problem. We represent the Earth model as a continuously varying background with an embedded salt body. The salt geometry is described by the zero contour of a level-set function, which in turn is represented with a relatively small number of radial basis functions. This formulation includes some additional parameters such as the width of the basis functions and the smoothness of the Heaviside function. The latter is of particular importance as it controls the sensitivity to changes in the salt geometry. We propose a robust algorithm that adaptively chooses the required smoothness parameter and tested the method on a suite of idealized Earth models with different salt geometries. For a fixed and accurate background model, the level-set method is shown to give superior estimates of the salt geometry and is stable against a moderate amount of noise. Additional results demonstrate that is feasible to jointly estimate the background and the salt geometry.

To further develop the method as a viable alternative to conventional full-waveform inversion, tests on more realistic Earth models are needed. In particular, the joint estimation of the background model and salt geometry needs to be investigated further. Even when representing the level-set function
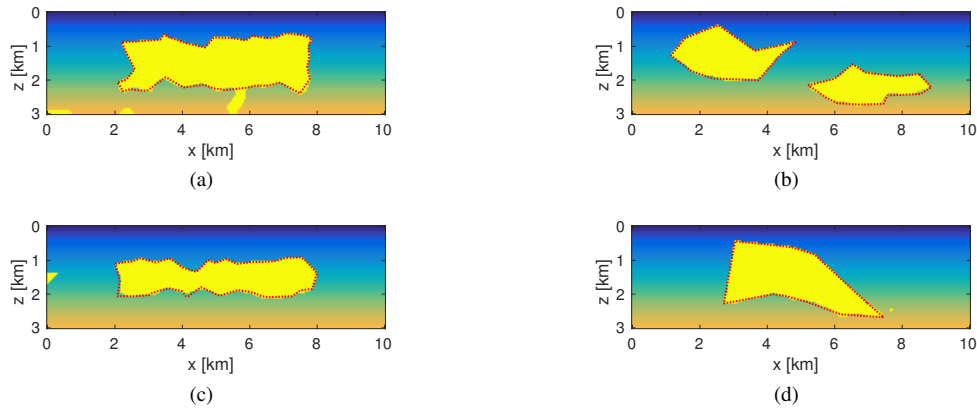
Fig. 10. Simultaneous reconstruction of salt and background with Parametric level-set full waveform inversion (PLS-FWI) on noisy data with SNR 10 *dB*. (a), (b), (c), (d) represent reconstructed model A, B, C, D respectively. Red dotted line shows the true geometry of salt.

with a finite basis, there are many level-set functions that result in the same salt geometry. To address this issue, additional regularization is needed. An often-used approach is to re-initialize the level-set function by solving an eikonal equation. In the parametric framework, this can be included by adding the discretized eikonal equation as a regularization term.

In this paper, we fixed RBF grid *a priori*. For very complex salt-geometries, this may no longer be feasible as it would require too many nodes for their accurate representation. An adaptive choice of the RBF grid may address this problem but it is not obvious how to refine the grid.

## ACKNOWLEDGMENT

## REFERENCES

[1] A. Aghasi, M. Kilmer, and E. L. Miller. Parametric level set methods for inverse problems. *SIAM Journal on Imaging Sciences*, 4(2):618–650, 2011.

[2] A. Y. Anagaw and M. D. Sacchi. Edge-preserving seismic imaging using the total variation method. *Journal of Geophysics and Engineering*, 9(2):138, 2012.

[3] A. Asnaashari, R. Brossier, S. Garambois, F. Audebert, P. Thore, and J. Virieux. Regularized seismic full waveform inversion with prior model information. *Geophysics*, 78(2):R25–R36, 2013.

[4] A. Bayliss and E. Turkel. Radiation boundary conditions for wave-like equations. *Communications on Pure and Applied Mathematics*, 33(6):707–725, 1980.

[5] P. Bharadwaj, W. A. Mulder, and G. G. Drijkoningen. Full waveform inversion with an auxiliary bump functional. *Geophysical Journal International*, 206(2):1076–1092, 2016.

[6] R. Brossier, S. Operto, and J. Virieux. Seismic imaging of complex onshore structures by 2D elastic frequency-domain full-waveform inversion. *Geophysics*, 74(6):WCC105–WCC118, 2009.

[7] M. D. Buhmann. Radial basis functions: theory and implementations. *Cambridge Monographs on Applied and Computational Mathematics*, 12:147–165, 2003.

[8] C. Bunks, F. M. Saleck, S. Zaleski, and G. Chavent. Multiscale seismic waveform inversion. *Geophysics*, 60(5):1457–1473, 1995.

[9] J. Carcione, G. C. Herman, and A. P. E. ten Kroode. Seismic modeling. *Geophysics*, 67(4):1304–1325, 2002.

[10] W. C. Chew and Q. H. Liu. Perfectly matched layers for elastodynamics: a new absorbing boundary condition. *Journal of Computational Acoustics*, 4(4):341–359, 1996.

[11] R. W. Clayton and B. Engquist. Absorbing boundary conditions for wave-equation migration. *Geophysics*, 45(5):895–904, 1980.

[12] Y. A. Erlangga and F. J. Herrmann. An iterative multilevel method for computing wavefields in frequency-domain seismic inversion. In *SEG Technical Program Expanded Abstracts*. Society of Exploration Geophysicists, 2008.

[13] O. G. Ernst and M. J. Gander. Why it is difficult to solve Helmholtz problems with classical iterative methods. In *Numerical Analysis of Multiscale Problems*, pages 325–363. 2012.

[14] E. Esser, L. Guasch, T. van Leeuwen amd A. Y. Aravkin, and F. J. Herrmann. Automatic salt delineation — Wavefield Reconstruction Inversion with convex constraints. In *SEG Technical Program Expanded Abstracts 2015*, pages 1337–1343. Society of Exploration Geophysicists, 2015.

[15] Odile Gauthier, Jean Virieux, and Albert Tarantola. Two-dimensional nonlinear inversion of seismic waveforms: Numerical results. *Geophysics*, 51(7):1387–1403, 1986.

[16] A. George and J. W.-H. Liu. *Computer Solution of Large Sparse Positive Definite Systems*. Prentice-Hall, Englewood Cliffs, NJ, 1981.

[17] Zhaohui Guo, Maarten V de Hoop, et al. Shape optimization and level set method in full waveform inversion with 3D body reconstruction. In *2013 SEG Annual Meeting*. Society of Exploration Geophysicists, 2013.

[18] Eldad Haber, Uri M Ascher, and Doug Oldenburg. On optimization techniques for solving nonlinear inverse problems. *Inverse Problems*, 16(5):1263–1280, 2000.

[19] B. Hustedt, S. Operto, and J. Virieux. Mixed-grid and staggered-grid finite-difference methods for frequency-domain acoustic wave modelling. *Geophysical Journal International*, 157(3):1269–1296, 2004.

[20] Churl-Hyun Jo, Changsoo Shin, and Jung Hee Suh. An optimal 9-point, finite-difference, frequency-space, 2-D scalar wave extrapolator. *Geophysics*, 61(2):529–537, 1996.

[21] H. Knibbe, W. A. Mulder, C. W. Oosterlee, and C. Vuik. Closing the performance gap between an iterative frequency-domain solver and an explicit time-domain scheme for 3D migration on parallel architectures. *Geophysics*, 79(2):S47–S61, 2014.

[22] B. N. Kuvshinov and W. A. Mulder. The exact solution of the time-harmonic wave equation for a linear velocity profile. *Geophysical Journal International*, 167(2):659–662, 2006.

[23] Winston Lewis, Bill Starr, Denes Vigh, et al. A level set approach to salt geometry inversion in full-waveform inversion. In *2012 SEG Annual Meeting*. Society of Exploration Geophysicists, 2012.

[24] Y. Lin and L. Huang. Acoustic- and elastic-waveform inversion using a modified total-variation regularization scheme. *Geophysical Journal International*, 200(1):489–502, 2014.

[25] Kurt J Marfurt. Accuracy of finite-difference and finite-element modeling of the scalar and elastic wave equations. *Geophysics*, 49(5):533–549, 1984.

[26] Charles A Micchelli. Interpolation of scattered data: distance matrices and conditionally positive definite functions. In *Approximation theory and spline functions*, pages 143–145. Springer, 1984.

[27] Dong-Joo Min, Changsoo Shin, R Gerhard Pratt, and Hai Soo Yoo. Weighted-averaging finite-element method for 2D elastic wave equations in the frequency domain. *Bulletin of the Seismological Society of America*, 93(2):904–921, 2003.

[28] W. A. Mulder, S. Osher, and J. A. Sethian. Computing interface motion in compressible gas dynamics. *Journal of Computational Physics*, 100(2):209–228, 1992.

[29] W. A. Mulder and R.-E. Plessix. Time-versus frequency-domain modelling of seismic wave propagation. In *64th EAGE Conference & Exhibition*, 2002.

[30] Jorge Nocedal. Updating quasi-Newton matrices with limited storage. *Mathematics of computation*, 35(151):773–782, 1980.

[31] S. Operto, J. Virieux, P. Amestoy, J.-Y. LExcellent, L. Giraud, and H. Ben Hadj Ali. 3D finite-difference frequency-domain modeling of visco-acoustic wave propagation using a massively parallel direct solver: A feasibility study. *Geophysics*, 72(5):SM195–SM211, 2007.

[32] S. Osher and R. P. Fedkiw. Level set methods: an overview and some recent results. *Journal of Computational Physics*, 169(2):463–502, 2001.

[33] Stanley Osher and James A Sethian. Fronts propagating with curvature-dependent speed: algorithms based on hamilton-jacobi formulations. *Journal of computational physics*, 79(1):12–49, 1988.

[34] R.-E. Plessix. A review of the adjoint-state method for computing the gradient of a functional with geophysical applications. *Geophysical Journal International*, 167(2):495–503, 2006.

[35] R.-E. Plessix, G. Chavent, and Y.-H. De Roeck. Waveform inversion of reflection seismic data for kinematic parameters by local inversion. *SIAM Journal on Scientific Computing*, 20(3):1033–1052, 1999.

[36] M. J. D. Powell. Radial basis functions for multivariable interpolation: a review. In *Algorithms for approximation*, pages 143–167. Clarendon Press, 1987.

[37] R Gerhard Pratt. Seismic waveform inversion in the frequency domain, part 1: Theory and verification in a physical scale model. *Geophysics*, 64(3):888–901, 1999.

[38] R Gerhard Pratt, Changsoo Shin, and GJ Hick. Gauss–Newton and full Newton methods in frequency–space seismic waveform inversion. *Geophysical Journal International*, 133(2):341–362, 1998.

[39] C. D. Riyanti, Y. A. Erlangga, R.-E. Plessix, W. A. Mulder, C. Vuik, and C. Oosterlee. A new iterative solver for the time-harmonic wave equation. *Geophysics*, 71(5):E57–E63, 2006.

[40] Leonid I Rudin, Stanley Osher, and Emad Fatemi. Nonlinear total variation based noise removal algorithms. *Physica D: Nonlinear Phenomena*, 60(1):259–268, 1992.

[41] Yousef Saad. *Iterative methods for sparse linear systems*. Siam, 2003.

[42] F. Santosa and W. W. Symes. *An analysis of least-squares velocity inversion*. Geophysical monograph series. Society of exploration geophysicists, 1989.

[43] M. Schmidt. minfunc: unconstrained differentiable multivariate optimization in matlab, 2005.

[44] M. W. Schmidt, E. Van Den Berg, M. P. Friedlander, and K. P. Murphy. Optimizing costly functions with simple constraints: A limited-memory projected quasi-Newton algorithm. In *AISTATS*, volume 5, page 2009, 2009.

[45] C. Shin and H. Sohn. A frequency-space 2-D scalar wave extrapolator using extended 25-point finite-difference operator. *Geophysics*, 63(1):289–296, 1998.

[46] C. Da Silva and F. J. Herrmann. *A unified 2D/3D software environment for large-scale time-harmonic full-waveform inversion*, pages 1169–1173. 2016.

[47] L. Sirgue and R. G. Pratt. Efficient waveform inversion and imaging: A strategy for selecting temporal frequencies. *Geophysics*, 69(1):231–248, 2004.

[48] I Štekl and R Gerhard Pratt. Accurate viscoelastic modeling by frequency-domain finite differences using rotated operators. *Geophysics*, 63(5):1779–1794, 1998.

[49] W. W. Symes. The seismic reflection inverse problem. *Inverse Problems*, 25(12):123008, 2009.

[50] W. W. Symes. Seismic inverse poblems: recent developments in theory and practice. In A.K. Louis, S. Arridge, and B. Rundell, editors, *Proceedings of the Inverse Problems from Theory to Applications Conference*, pages 2–6. IOP Publishing, 2014.

[51] W. W. Symes and J. J. Carazzone. Velocity inversion by differential semblance optimization. *Geophysics*, 56(5):654–663, 1991.

[52] Christopher KW Tam and Jay C Webb. Dispersion-relation-preserving finite difference schemes for computational acoustics. *Journal of computational physics*, 107(2):262–281, 1993.

[53] T. van Leeuwen and F. J. Herrmann. Mitigating local minima in full-waveform inversion by expanding the search space. *Geophysical Journal International*, 195(1):661–667, 2013.

[54] J. Virieux, V. Etienne, V. Cruz-Atienza, R. Brossier, E. Chaljub, O. Coutant, S. Garambois, D. Mercerat, V. Prieux, S. Operto, A. Ribodetti, and J. Tago. Modelling seismic wave propagation for geophysical imaging. In Masaki Kanao, editor, *Seismic Waves – Research and Analysis*. InTech, 2012.

[55] J. Virieux and S. Operto. An overview of full-waveform inversion in exploration geophysics. *Geophysics*, 74(6):WCC1–WCC26, 2009.

[56] S. Wang, M. V. de Hoop, and J. Xia. On 3D modeling of seismic wave propagation via a structured parallel multifrontal direct Helmholtz solver. *Geophysical Prospecting*, 59(5):857–873, 2011.

[57] H. Wendland. Piecewise polynomial, positive definite and compactly supported radial functions of minimal degree. *Advances in Computational Mathematics*, 4(1):389–396, 1995.

[58] X. Zhang, K. Z. Song, M. W. Lu, and X. Liu. Meshless methods based on collocation with radial basis functions. *Computational Mechanics*, 26(4):333–343, 2000.
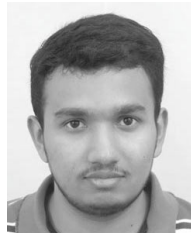
**Ajinkya Kadu** was born in Bhilai, India, on April 20, 1993. He received BSc. and MSc. degree in Aerospace Engineering from the Indian Institute of Technology, Bombay, India, in 2015. He is working towards the PhD. degree at Mathematical Institute of Utrecht University, The Netherlands. His PhD. is part of 'Computational Sciences for Energy Research', a joint partnership between Shell and NWO/FOM. His research interests include computational imaging, full-waveform inversion and meta-heuristic optimization.

**Tristan van Leeuwen** received his BSc. and MSc. in Computational Science from Utrecht University. He obtained his PhD. in geophysics at Delft University in 2010. After spending some time as a postdoctoral researcher at the University of British Columbia in Vancouver, Canada and the Centrum Wiskunde & Informatica in Amsterdam, the Netherlands, he returned to Utrecht University in 2014 as an assistant professor at the mathematical institute. His research interests include: inverse problems, computational imaging, tomography and numerical optimization.

**Wim Mulder** received a MSc degree in Astronomy with honours in 1980 and a PhD degree in 1985 from Leiden. He worked as a postdoc in the numerical analysis group of the Computer Science Department at Stanford University until 1987, followed by two years as an assistant professor of computational and applied mathematics at UCLA. He joined Shell in 1989 and worked on problems in reservoir flow simulation and seismic and electromagnetic modelling and inversion. Since 2005, he also holds a part-time professorship in the Department of Geoscience & Engineering at Delft University of Technology.